

Remodeling of Tumor Microenvironment by Tumor-Targeting Nanozymes Enhances Immune Activation of CAR T Cells for Combination Therapy

Lipeng Zhu, Jie Liu, Guangyu Zhou, Tzu-Ming Liu, Yunlu Dai, Guangjun Nie, and Qi Zhao*

Targeting B7-H3 chimeric antigen receptor (CAR) T cells has antitumor potential for therapy of non-small cell lung cancer (NSCLC) in preclinical studies. However, CAR T cell therapy remains a formidable challenge for the treatment of solid tumors due to the heterogeneous and immunosuppressive tumor microenvironment (TME). Nanozymes exhibit merits modulating the immunosuppression of the tumor milieu. Here, a synergetic strategy by combination of nanozymes and CAR T cells in solid tumors is described. This nanozyme with dual photothermal-nanocatalytic properties is endowed to remodel TME by destroying its compact structure. It is found that the B7-H3 CAR T cells infused in mice engrafted with the NSCLC cells have superior antitumor activity after nanozyme ablation of the tumor. Importantly, it is found that the changes altered immune-hostile cancer environment, resulting in enhanced activation and infiltration of B7-H3 CAR T cells. The first evidence that the process of combination nanozyme therapy effectively improves the therapeutic index of CAR T cells is presented. Thus, this study clearly supports that the TME-immunomodulated nanozyme is a promising tool to improve the therapeutic obstacles of CAR T cells against solid tumors.

granted breakthrough therapy designation to anti-B7-H3 antibody 8H9 for treatment of pediatric patients in 2017.^[6] Adoptive cell therapy of engineered T cells with chimeric antigen receptors (CARs) represents an attractive and innovative strategy for cancer treatment.^[7–9] Recently, we reported that the B7-H3 CAR-based 8H9 had antitumor potential for therapy of non-small cell lung cancer (NSCLC) in the preclinical studies.^[10] However, in solid tumors, one major obstacle to limit CAR T cell therapy is tumor microenvironment (TME) as formidable barriers.^[11–13] Intrinsic TME, including a complex network of plastic stroma, immunosuppressive cells, cytokines, and inhibitory immune checkpoints, attenuates CAR T cell response and infiltration.^[14–18] To combat immunosuppression of CAR T cell therapy, recent efforts have been made to improve CAR T cell potency by therapeutic approaches to overcome the current roadblocks in CAR T cell therapy through

increasing CAR T cell persistence, overcoming tumor heterogeneity or immune checkpoint inhibition.^[19–22] Nanotechnology is used to solve the problems of CAR T therapy by making nanoparticles that deliver liposome-based immunomodulatory drugs and directly modulate CAR T cells with synthetic DNA nanocarriers.^[23,24] However, compensatory mechanisms often enable tumors to develop resistance against CAR T cells. New strategies are still required to remodel the tumor milieu that impede effective CAR T cell trafficking to solid tumors.

As an emerging efficient modality, nanozymes with natural enzyme-like activities have been extensively explored to regulate TME by initiating intratumoral nanocatalytic chemical reactions with minimized harmful side effects.^[25–29] A typical nanozyme triggers cascade nanocatalytic tumor therapy (NCT) which converts endogenous hydrogen peroxide (H₂O₂) to generate hydroxyl radicals (·OH), a kind of highly toxic reactive oxygen species (ROS), through a catalytic reaction catalyzed by metal ions. The generated highly toxic ·OH species induce cancer cell death by damaging intracellular biomolecule substances (such as proteins, lipids, and DNA) or triggering programmed cell apoptosis. Copper (Cu)-based nanomaterials have frequently been used as efficient nanocatalysts because of Cu's wide range of accessible oxidation states.^[30] Additionally, Cu-based nanomaterials with high near-infrared (NIR) absorption make them useful for photothermal therapy (PTT), which


1. Introduction

B7-H3, a novel immune checkpoint molecule, plays important roles in tumor immune evasion and metastasis, making it an attractive oncoimmunology target in multiple types of tumors.^[1–5] Specifically, the United States Food and Drug Administration has

L. Zhu, J. Liu, G. Zhou, Prof. T. Liu, Prof. Y. Dai, Prof. Q. Zhao
Cancer Centre
Institute of Translational Medicine
Faculty of Health Sciences
University of Macau
Macau SAR 999078, China
E-mail: qizhao@um.edu.mo

L. Zhu, J. Liu, G. Zhou, Prof. T. Liu, Prof. Y. Dai, Prof. Q. Zhao
MoE Frontiers Science Center for Precision Oncology
University of Macau
Macau SAR 999078, China

Prof. G. Nie
CAS Key Laboratory for Biomedical Effects of Nanomaterials
& Nanosafety
National Center for Nanoscience and Technology
Beijing 100190, China

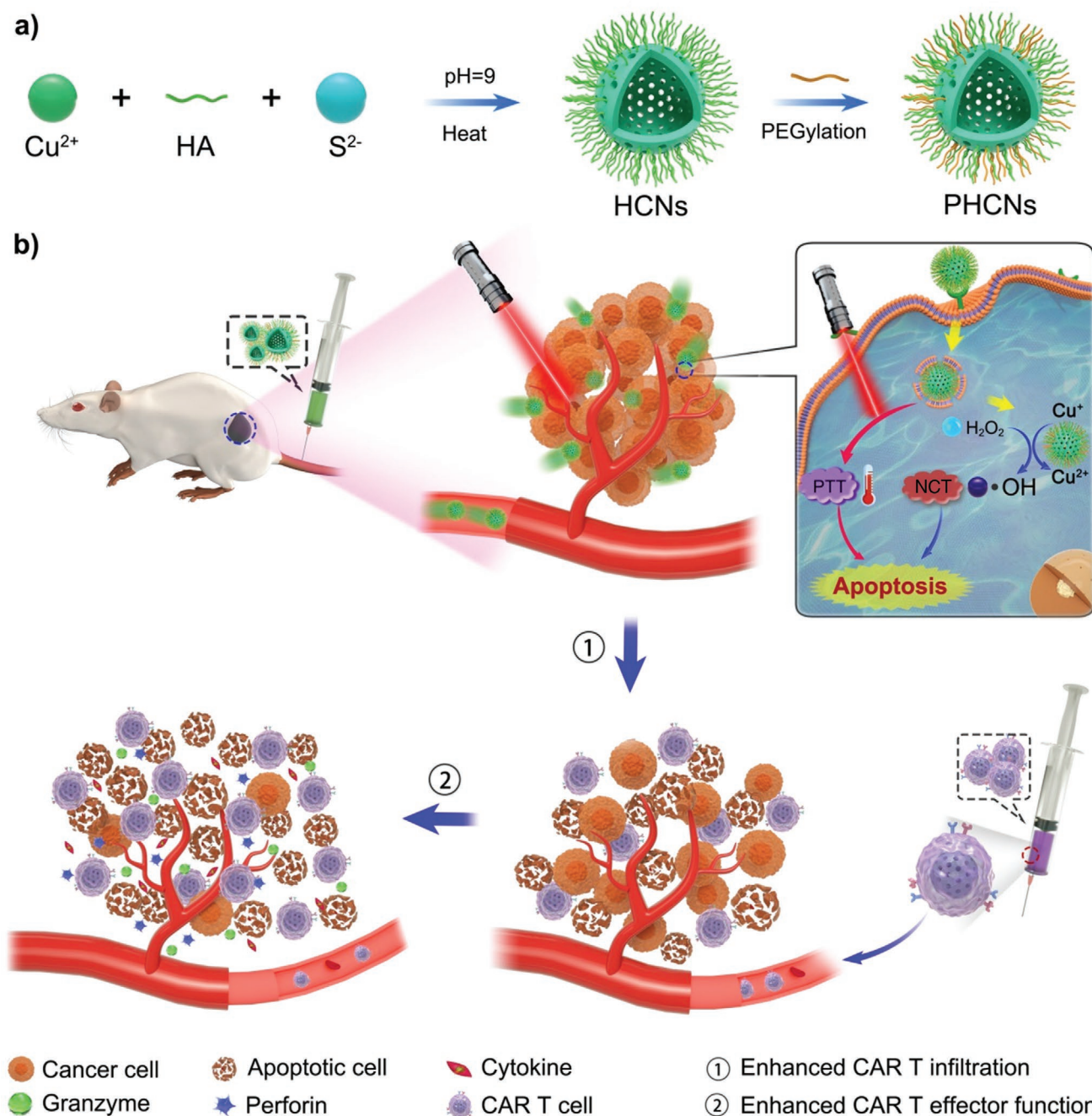
 The ORCID identification number(s) for the author(s) of this article can be found under <https://doi.org/10.1002/smll.202102624>.

DOI: 10.1002/smll.202102624

eradicates tumor cells with high selectivity and low systemic toxicity by converting light energy into localized heat upon NIR laser irradiation.^[31–35] Therefore, the design and development of Cu-based nanozymes with PTT properties in the NIR region have broad prospects.

In the research described here, we exploited a nanozyme combination strategy that can block immunosuppression of TME and simultaneously stimulate CAR T cells. As a targeting ligand, hyaluronic acid (HA), a natural anionic polysaccharide,

can recognize abundant HA receptors (CD44) on specific tumor cells.^[36] Herein, a tumor-specific HA@Cu_{2-x}S-PEG (PHCN) nanozyme was synthesized by the sacrificial template chemical transformation method. To improve antitumor effects of B7-H3 CAR T therapy, the PHCN-based nanosystem was designed to enhance the infiltration and effector function of CAR T cells (Scheme 1). Photothermal-nanocatalytic (PNC) synergistic effects of nanozymes effectively reverse the immune-hostile cancer environment and thereby decrease tumor resistance to



Scheme 1. a) Preparation procedure of PHCNs. b) Schematic illustration of nanozyme-mediated PNC effects for enhanced infiltration and effector function of CAR T cells in solid tumors.

CAR T cells. The crucial aspect of PHCN is to trigger ROS production in the TME and induce PNC synergistic effect resulting in tumor cell killing, which causes the release of tumor-specific antigen from tumor cells, facilitating to activate the effector function of CAR T cells. Meanwhile, we observed CAR T cells are able to effectively infiltrate tumor lesions due to destruction of the tumor extracellular matrix by nanozyme-induced PNC effect under laser irradiation. In the preclinical models of NSCLC, we confirmed that nanozyme administration doubled tumor eradication and the overall survival compared with conventional CAR T-cell therapy alone.

2. Results and Discussion

2.1. Preparation and Characterization of Nanozymes

Here, HA@Cu_{2-x}S (HCNs) were synthesized by reacting CuCl₂ and Na₂S using HA as the capping stabilizer through the conjugation of carboxyl groups of HA with Cu ions. Monodispersed HCNs with a hollow structure and spherical shape exhibited an average diameter of approximately 125 nm (Figure 1a,b; Figure S1, Supporting Information). The lattice spacing (d-spacing) of the (102) plane was approximately 0.3086 nm (Figure 1c). The HCNs crystal structure was confirmed by a selected area electron diffraction pattern (Figure S2, Supporting Information). The UV-vis absorption spectra of HCNs solutions (Figure 1d) showed strong absorbance in the NIR region. The components of the HCNs were further confirmed through energy-dispersive spectroscopy (EDS) (Figure S3, Supporting Information) and elemental mapping analysis (Figure 1e-g), both of which indicated the presence of Cu and S signals. The X-ray diffraction (XRD) patterns (Figure 1h) indicated that the peaks of the HCNs were completely coincident with the covellite phase CuS (JCPDS file number 06-0464). The analysis of the X-ray photoelectron spectroscopy (XPS data, Figure 1i) revealed the existence of Cu⁺/Cu²⁺ due to the peaks of 952.1/953.5 and 932.3/933.7 eV, respectively, in accordance with the Cu 2p_{1/2} and Cu 2p_{3/2} levels. The XPS (Figure 1j) displayed the distribution of C, O, S, N, and Cu in HCNs, further demonstrating the presence of HA coating. The peaks of C 1s (Figure 1k) confirmed the presence of HA, and Fourier transform infrared spectroscopy (FT-IR) spectra (Figure 1l) further proved this result. To further improve stability and biocompatibility, PEG was introduced to modify the HCNs to construct multifunctional HA@Cu_{2-x}S-PEG nanozymes (PHCNs). The zeta potential dropped from -21.75 mV down to -16.2 mV after PEG modification (Figure 1m), indicating the successful modification of PEG. Moreover, the PHCNs exhibited excellent stability in the different solutions (Figure S4, Supporting Information), making them suitable for further biological applications.

2.2. Dual Photothermal and Nanocatalytic Properties of PHCNs

Due to the strong NIR absorption, the PHCNs showed excellent concentration- and laser power density-dependent photothermal properties under laser irradiation (Figure 2a; Figure S5,

Supporting Information). The temperature of the PHCNs solutions markedly increased under laser irradiation, while no obvious temperature elevation of phosphate-buffered saline (PBS) was observed (Figure 2a,b). The PHCNs exhibited a high photothermal conversion efficiency of 52.81%, better than most of the reported nanomaterials (Figure S6, Supporting Information), and excellent photothermal stability (Figure S7, Supporting Information). The peroxidase-like catalytic performances of the PHCNs were investigated in an H₂O₂ substrate system. We found that the steady-state kinetics fitted the typical Michaelis-Menten steady-state kinetics model in the tested concentration range of H₂O₂ (Figure 2c). The important enzyme parameters *K_m* and *V_{max}* values for the PHCNs were listed in Table S1, Supporting Information, which indicated that the PHCNs had higher catalytic activity compared to the reported nanozymes. Meanwhile, the methylene blue (MB) degradation method was used to detect the generation of ·OH. The nanocatalytic activities of PHCNs were confirmed to convert decomposition of H₂O₂ into generate ·OH (Figure S8a, Supporting Information). The PHCNs displayed the nanocatalytic property in an H₂O₂-dependent manner (Figure 2d). The generation of ·OH by the PHCNs under 808 nm laser irradiation or higher temperature was enhanced (Figure S8a,b, Supporting Information), suggesting that photothermal could promote the catalytic rate. Additionally, cellular uptake of the PHCNs was measured by inductively coupled plasma mass spectrometry (ICP-MS). As shown in Figure 2e, PHCNs were effectively internalized by A549 cells due to HA-mediated active targeting of the endocytosis effect. The amount of PHCNs in cells markedly decreased under HA preincubation because free HA inhibited HA-mediated endocytosis by blockade of CD44 receptors.^[37] No obvious cytotoxicity of the PHCNs toward noncancerous HUVECs was found (Figure S9, Supporting Information), which indicated that PHCNs have good biocompatibility. However, a cell inhibition rate of PHCNs was observed because the catalytic effect of PHCNs could generate ·OH that induced tumor cell apoptosis. We observed that the photothermal effect enhanced NCT-mediated higher ·OH generation in cancer cells (Figure 2f). The cell survival rate of cells irradiated with laser irradiation was significantly lower than that of cells without laser irradiation (Figure 2g), suggesting that photothermal enhanced the anticancer therapeutic effect of NCT. Fluorescence staining of living/dead cells further demonstrated that PHCNs displayed the effective PNC synergistic ablation of cancer cells (Figure 2h).

2.3. In Vivo Dual-Modal Imaging of PHCNs

To detect dynamic distribution of PHCNs in tumors, a photoacoustic (PA) imaging method was employed to monitor the signals at different times based on the excellent PA data in vitro (Figure 3a). After intravenous injection, the PA signals of the tumor region increased with increasing time and reached a peak at 12 h (Figure 3b,c). The results suggested that PHCNs could effectively accumulate in tumors through an active targeting effect. The high biodistribution of PHCNs in tumor tissues (Figure S10, Supporting Information) was further confirmed using ICP-MS. Then, photothermal imaging could

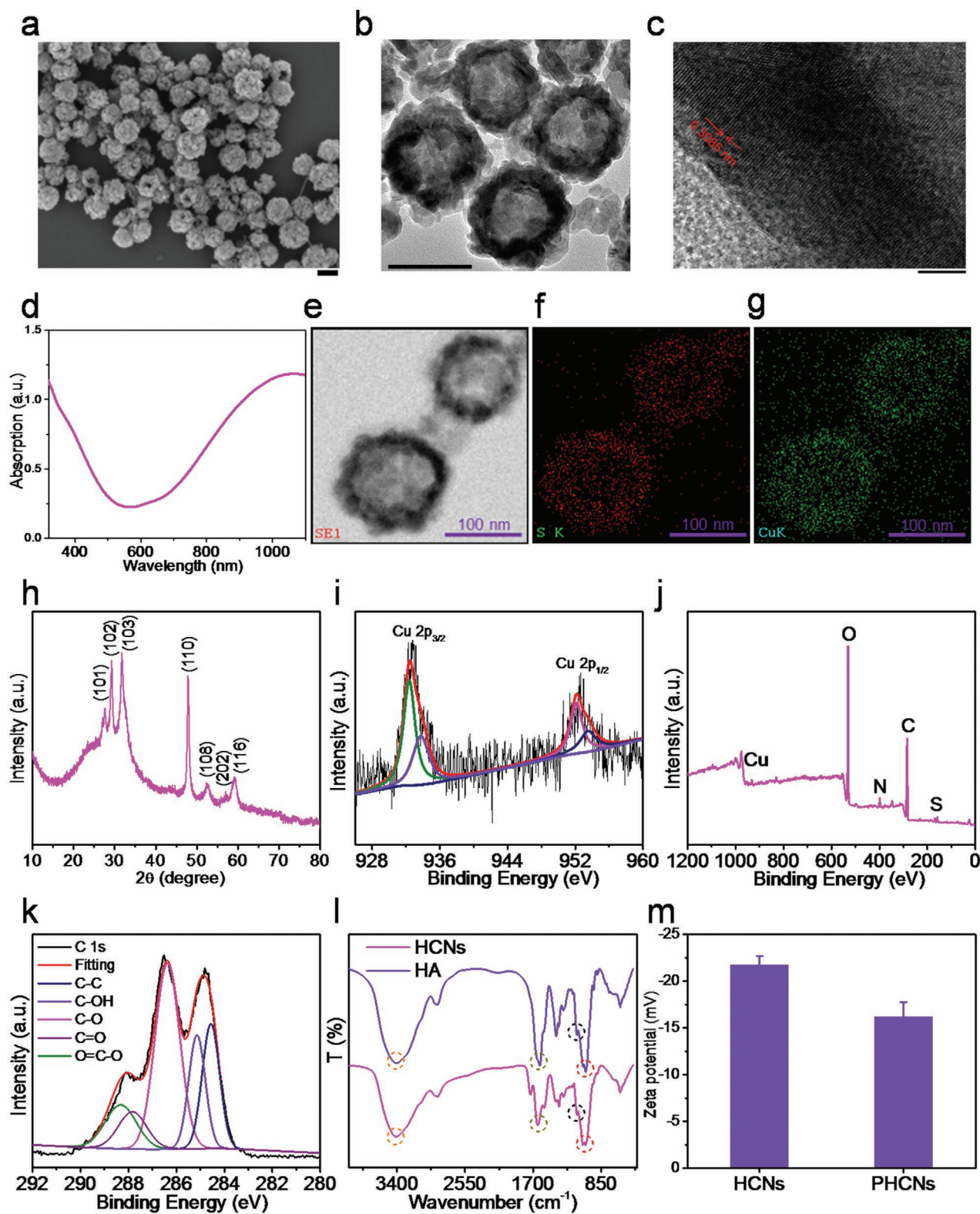


Figure 1. Characterization of nanozymes. a) SEM and b) TEM images of HCNs. Scale bar: 100 nm. c) HRTEM images of HCNs. Scale bar: 5 nm. d) UV-vis spectrum of HCNs. e–g) EDS elemental mapping of HCNs. h) XRD patterns of HCNs. i) High-resolution Cu 2p in HCNs. j) XPS characterization and k) C 1s of HCNs. l) FT-IR spectra of HA and HCNs. m) Zeta potential of HCNs and PHCNs by DLS measurement.

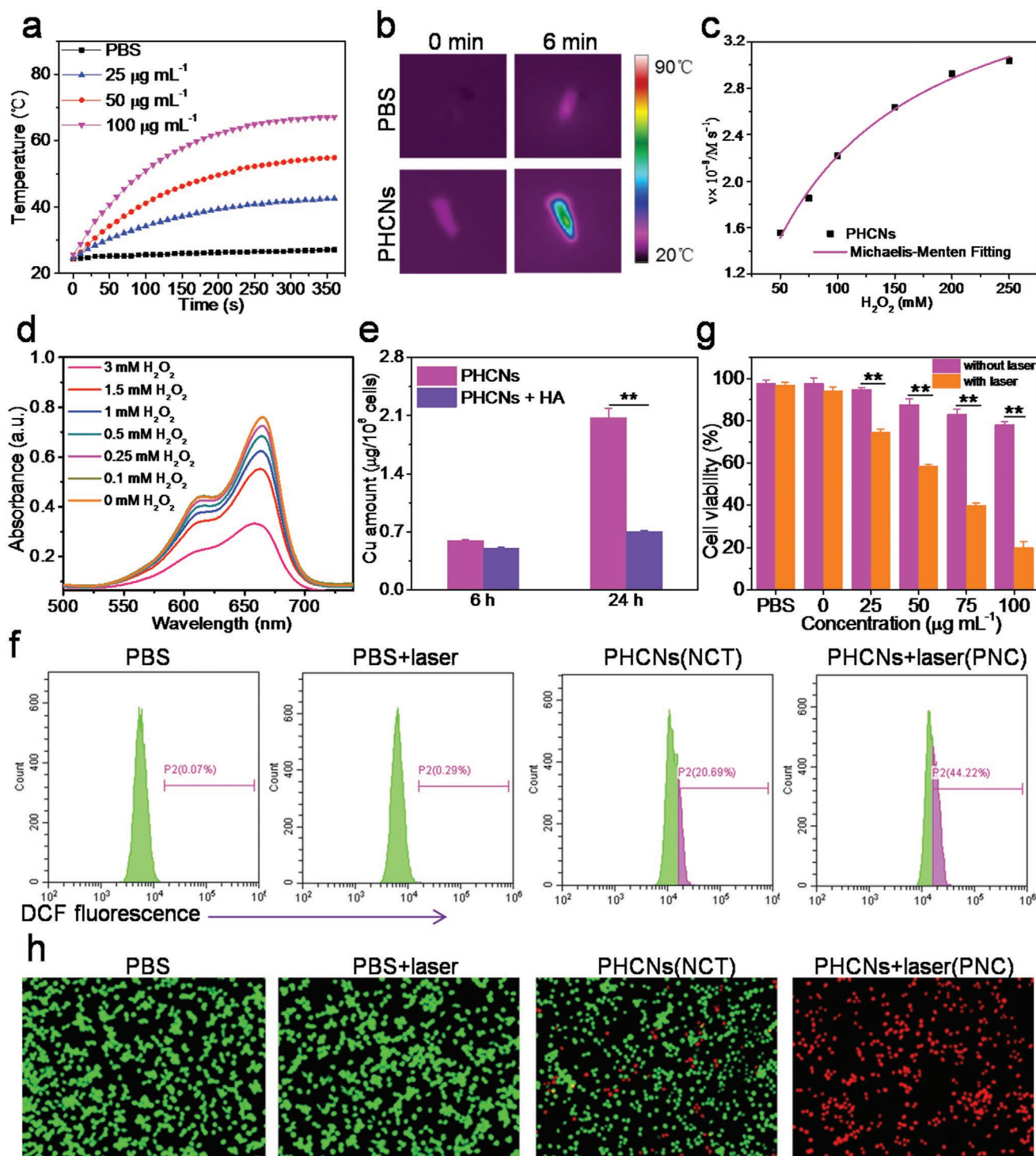


Figure 2. Nanocatalytic and photothermal properties of PHCN nanozyme. a) Temperature elevation curves of PBS and different concentrations of PHCNs exposed to a NIR laser for 6 min. b) Thermographic images of PBS and PHCNs at different intervals under laser irradiation. c) Michaelis–Menten kinetics plot of the PHCNs. d) MB degradation in PHCNs treated with different H₂O₂ concentrations. e) Cellular internalized amounts of PHCNs from different treatments measured by ICP-MS. f) Intracellular ROS content is analyzed by flow cytometry after different treatments using DCF as a ROS sensor. g) Viability of A549 cells incubated with different concentrations of PHCNs and treated with/without laser irradiation. h) Fluorescence images of cells after different treatments; the cells are costained with calcein-AM (green, living cells) and propidium iodide (red, dead cells). The *p* values are analyzed using the Log-rank (Mantel-Cox) test. Data are presented as the mean ± standard error of the mean. **p* < 0.05, ***p* < 0.01, ****p* < 0.001.

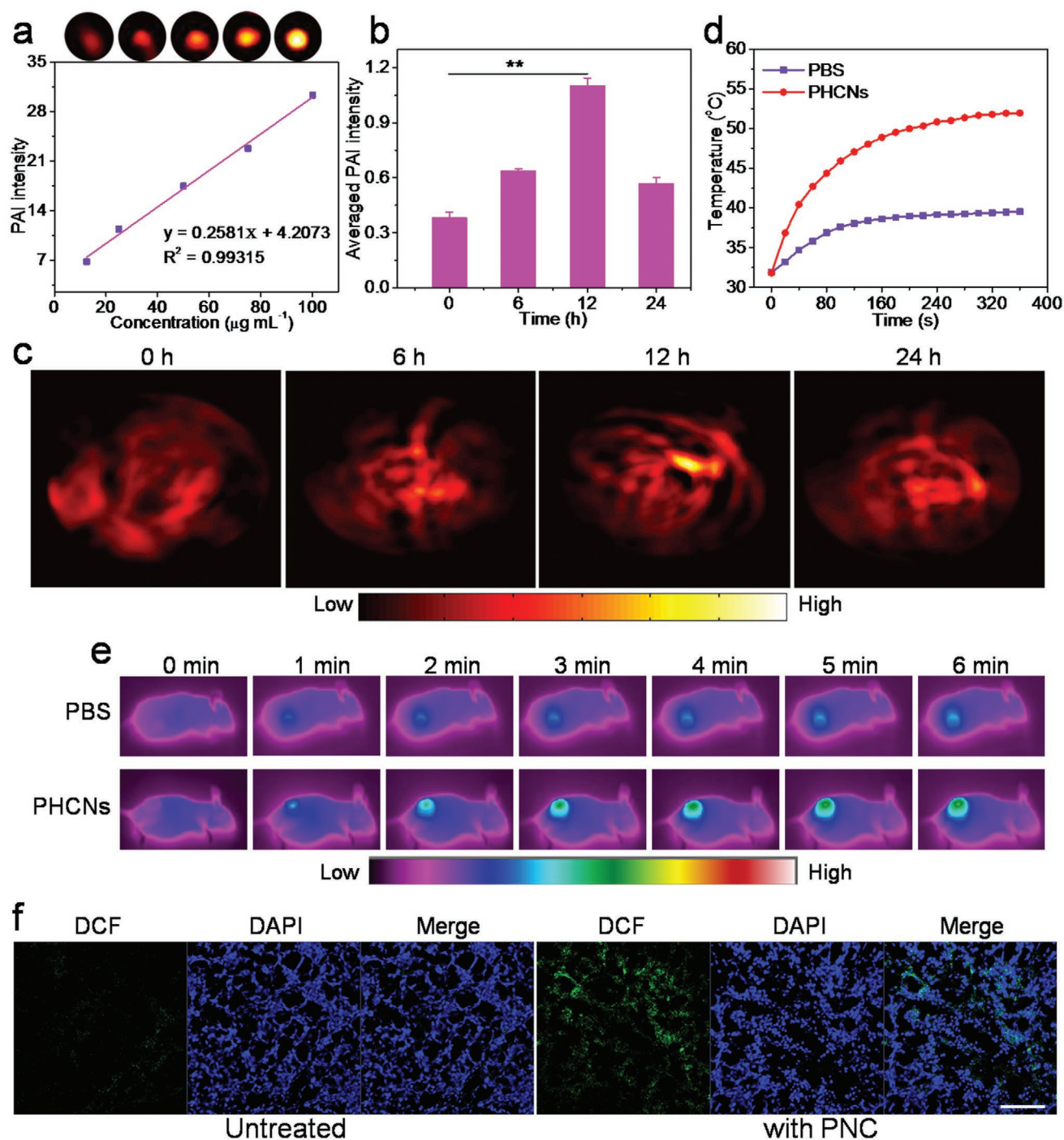


Figure 3. Near-infrared PA imaging of PHCN nanozyme for visualization tracing. a) The in vitro PA value of PHCNs as a function of the concentrations of PHCNs. The averaged PAI intensity (b) and PA imaging (c) of mice bearing tumors intravenously injected with PHCNs at 0, 6, 12, and 24 h. The p values are analyzed using the Log-rank (Mantel-Cox) test. Data are presented as the mean \pm standard error of the mean. $*p < 0.05$, $**p < 0.01$, $***p < 0.001$. Temperature elevation curves (d) and infrared photothermal images (e) of tumor-bearing mice measured after intravenous injection of PBS and PHCNs plus further laser irradiation. f) DCF staining of tumor tissues from different groups. Scale bar: 100 μm .

be used to test the temperature variation of the tumor by an infrared thermal camera. After injection for 12 h, the temperature of the tumor region gradually increased with increasing irradiation time under NIR laser power density, and the temperature significantly increased to 51.97 $^{\circ}\text{C}$ within 6 min

(Figure 3d,e). In contrast, the temperature of the tumor under PBS treatment was not markedly elevated. Moreover, strong DCF green fluorescence intensity was detected with PNC treatment compared to control tumors, suggesting that the PHCN-mediated PNC effect would result in high ROS production in

the tumor site (Figure 3f). Therefore, the results showed that PHCNs could effectively enrich tumor and generate excellent photothermal effects in vivo.

2.4. Nanozymes Reverse Tumor Resistance to CAR T Cells by Modulating Tumor Cells

In our hypothesis, nanozyme-induced PNC effect could mediate immune activation of CAR T cells by alteration of tumor immunosuppression. To analyze the mechanism of activation of CAR T cells, we generated the B7-H3 CAR derived from an anti-B7-H3 antibody 8H9 that has been shown to preferentially bind tumor tissues and has been safely used in humans in early-phase clinical trials. By lentiviral transduction, B7-H3 CAR was expressed on the surface of T cells that were isolated from healthy human peripheral blood mononuclear cells (PBMCs). The expression rate of the B7-H3 CAR on T cells was determined to be approximately 60% (Figure 4a). The in vitro cytotoxicity of B7-H3 CAR T cells was evaluated against B7-H3-positive NSCLC cells (A549). As shown in Figure 4b, the antitumor lytic activity of B7-H3 CAR T cells was significantly enhanced when A549 cells were pretreated with nanozyme-mediated PNC effect.

To avoid nanozyme toxicity to CAR T cells, the remaining nanozymes in the supernatants were carefully removed from the tumor cells. Then, target tumor cells were subsequently treated with B7-H3 CAR T cells. We confirmed that the PHCNs at different concentrations did not show obvious toxicity to CAR T cells in the cytotoxicity studies (Figure 4c). Although minor nanozymes might have remained, we did not find that the remaining nanozymes impaired overall activation of CAR T cells in the subsequent assays.

To exploit how nanozymes drive CAR T cell therapy, we assessed the activations and differentiation markers of CAR T cells against target A549 cells without/with nanozyme-mediated PNC pre-treatment. First, we examined the proliferation percentage of B7-H3 CAR T cells that were in contact with target cells without/with nanozyme treatment. After co-incubation, B7-H3 CAR T cells exhibited increased proportion in nanozyme-treatment group compared with the non-nanozyme treated group (Figure 4d,e). Importantly, nanozyme promoted more amounts of CD8⁺ CAR T cells, known as the major population in killing tumor cells, than non-nanozyme treatment (Figure 4f,g). Second, the proinflammatory cytokines are essential for the CAR T cell potency. In nanozyme-treated group, B7-H3 CAR T cells produced markedly higher amounts of key cytokines, including interferon- γ (IFN- γ) and tumor

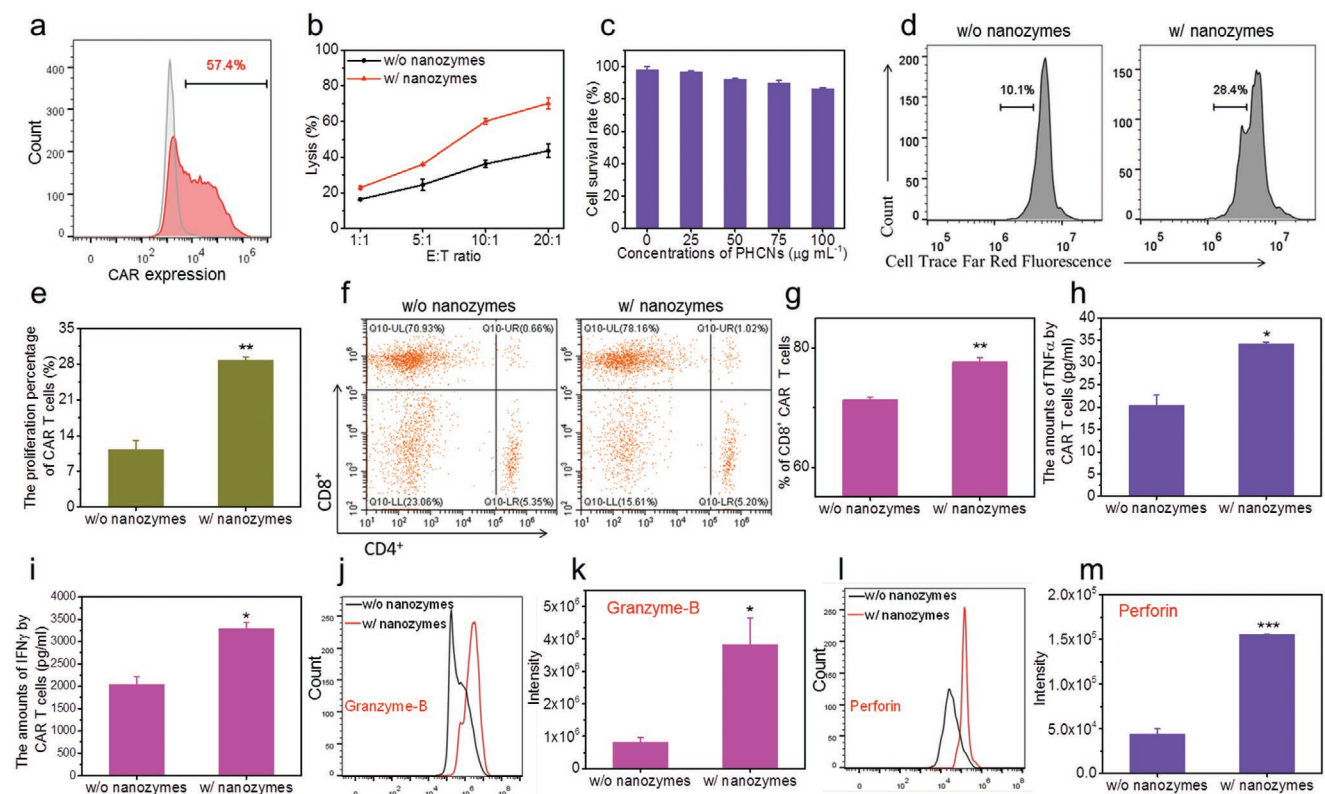


Figure 4. In vitro immunomodulation of B7-H3 CAR T cells with nanozyme-mediated PNC altering tumor cell resistance. a) CAR B7-H3 expression on T cells after two weeks of culture. b) Lysis rate of A549 cells without/with nanozyme-mediated PNC treatment after co-incubation CAR T cells under different E:T ratios. c) Viability of CAR T cells treated with different concentrations of PHCNs for 24 h. d) Flow cytometry analysis and e) the proliferation percentage of CAR T cells labeled with cell trace far red fluorescence after without/with nanozyme treating A549 cells. Representative proportions (f–g) of CD8⁺ CAR T cells measured by flow cytometry after co-cultured A549 cells without/with nanozyme treatment. h) The levels of TNF- α and i) IFN- γ released from CAR T cells. The levels of j–k) granzyme-B and l–m) perforin released from CAR T cells. The *p* values are analyzed using the Log-rank (Mantel-Cox) test. Data are presented as the mean \pm standard error of the mean. **p* < 0.05, ***p* < 0.01, ****p* < 0.001.

necrosis factor-alpha (TNF- α) compared with CAR T cells alone (Figure 4h,i). Third, a hallmark of CAR T cell activation is degranulation in which lytic granule contents (perforin and granzymes) are released onto the surface of the target cells. Significant increases in granzyme-B (Figure 4j,k) and perforin (Figure 4l,m) were observed in CAR T cells in the nanozyme treatment group. Finally, in a transwell migration assay, B7-H3 CAR T cells and A549 tumor cells were seeded at upper and lower chambers, respectively. CAR T cell migration was significantly enhanced after A549 cells were pretreated with nanozymes (Figure S11, Supporting Information). We speculate that tumor-specific B7-H3 antigen released from A549 cells by nanozyme-mediated PNC effect could further activate and recruit B7-H3 CAR T cells.

Our results demonstrated that nanozymes altered tumor cells to be susceptible to CAR T cell killing. The release of tumor-specific antigens by PNC effect stimulates CAR T cells and subsequently enhances CAR T cell effector function. The key cytokine levels and T cell degranulation were enhanced.

2.5. Nanozymes Improves In Vivo CAR T Therapy by Remodeling TME

The in vivo antitumor efficacy of nanozymes and B7-H3 CAR T cells therapy was evaluated using xenograft mouse models of NSCLC (A549). Subcutaneous xeno-transplanted tumor models were established in NOD/SCID mice. Mice-bearing tumors were intravenously injected with PHCNs and then laser-irradiated. After treatment, mice were intravenously administered 0.5×10^7 B7-H3 CAR T cells. Then the survival rate of mice and the tumor size was monitored by caliper measurement after treatment. The combination of CAR T cells and PHCNs with irradiated treatment completely suppressed the tumor growth within 15 days (Figure 5a,b, Figure S12, Supporting Information) and significantly prolonged the survival rate of mice (Figure 5c). As shown in the representative photographs, tumors in the combination treatment were not obvious after the synergistic treatment (Figure 5d,e). In contrast, either CAR T cells alone or CAR T cells plus non-irradiated PHCNs partially controlled tumor growth. The obvious destruction and apoptosis of tumor cells were observed under the combination of CAR T cells and PHCNs with irradiated treatment (Figure 5f,g). All results suggested that nanozyme-mediated PNC therapy effectively improved the therapeutic index of CAR T cell immunotherapy against solid tumors.

To further analyze the in vivo mechanism of action of B7-H3 CAR T cell treatment, the in vivo immune response of CAR T cells was evaluated in a xenograft tumor model of NOD/SCID mice bearing A549 cells subcutaneously. To evaluate tumor blood perfusion, in vivo tumor blood flow rates as the main index were measured by the laser speckle equipment. After 12 h injection of PHCNs in A549-xenografted mice, the tumor sites were irradiated. Then, the flow rates at the tumor sites were measured at the different time points as pre-irradiation, 0, 12, and 24 h post-irradiation. The blood flow rates were immediately increased at 0 h after PNC treatment (Figure S13, Supporting Information). Although the blood flow rates began to

slowly decrease at 12 and 24 h, the dropped values were obvious at 12 h. Meanwhile, we confirmed that nanozymes reached the highest density in tumors at 0 h (12 h post-PHCN injection) by a PA imaging assay (Figure 3b,c). The nanozymes were gradually metabolized in tumors after 12 h post-irradiation (24 h post-PHCN injection) (Figure S10, Supporting Information). To avoid the high density of nanozymes that might influence CAR T cells, we chose 12 h post-PNC treatment as the initial administration of CAR T cells. Therefore, the potential cytotoxicity of nanozymes will be carefully considered for designing the therapeutic schedules to achieve more rational combination therapy. As the results, CAR T cell injection 12 h post-PNC treatment may improve their infiltration in tumors. Five days later, tumor tissues were excised from mice that were undergoing treatment (Figure 6a). Intrinsic cytokine profiles and infiltrated T cell phenotypes in the TME were measured. In contrast to other control groups, elevated secretions of IFN- γ and TNF- α by CAR T cells were found after PHCNs with irradiated treatment (Figure 6b,c). In vivo results consistently demonstrated that nanozymes did not directly make obvious toxicity to CAR T cells. As the same treatment, we found the proportions of infiltrated CD8⁺ CAR T cells in tumors were obviously enhanced (Figure 6d,e, Figure S14, Supporting Information), which are important hints for T cell effector function in cancer immunity. To exploit whether the PHCNs with irradiated treatment on the tumors can increase the infiltration of B7-H3 CAR T cells, we performed fluorescent imaging analysis on tumors excised from the mice that were undergoing treatment. The vasculature of the tumor treated with PHCNs plus laser was dilated with reduced interstitial fluid pressure compared to control tumors (Figure 6f), suggesting that PNC effect could induce the alterations of tumor extracellular matrix. Immunofluorescence imaging further demonstrated the enhanced infiltration and accumulation of CAR T cells carrying the report gene in tumors after PHCNs with irradiated treatment (Figure 6g).

Therefore, these results suggest that the PHCN-mediated PNC therapy could promote the infiltration and effector function of CAR T cells in solid tumors.

2.6. Biocompatible Evaluation In Vivo

The on-target off-tumor toxicity is a major concern in CAR T cell therapy in the clinic.^[38] The in vivo potential toxicity of CAR T cells toward major organs was investigated by hematoxylin and eosin (H&E) staining. No obvious tissue damage or inflammatory lesions were observed in tissue slices (Figure S15, Supporting Information). The serum levels of serum aspartate transaminase (AST) and alanine transaminase (ALT) from all treatment groups showed that PHCNs had relatively low liver toxicity (Figure S16, Supporting Information). No significant weight loss was observed in mice (Figure S17, Supporting Information). No treatment-related adverse effects were observed in any group treated with B7-H3 CAR T cells. Our results showed that the B7-H3 CARs had minimal off-target toxicity, suggesting that regional tumor infiltration of B7-H3 CAR T cells may limit systemic toxicity by reducing the cross-reactivity of CAR T cells in other organs.

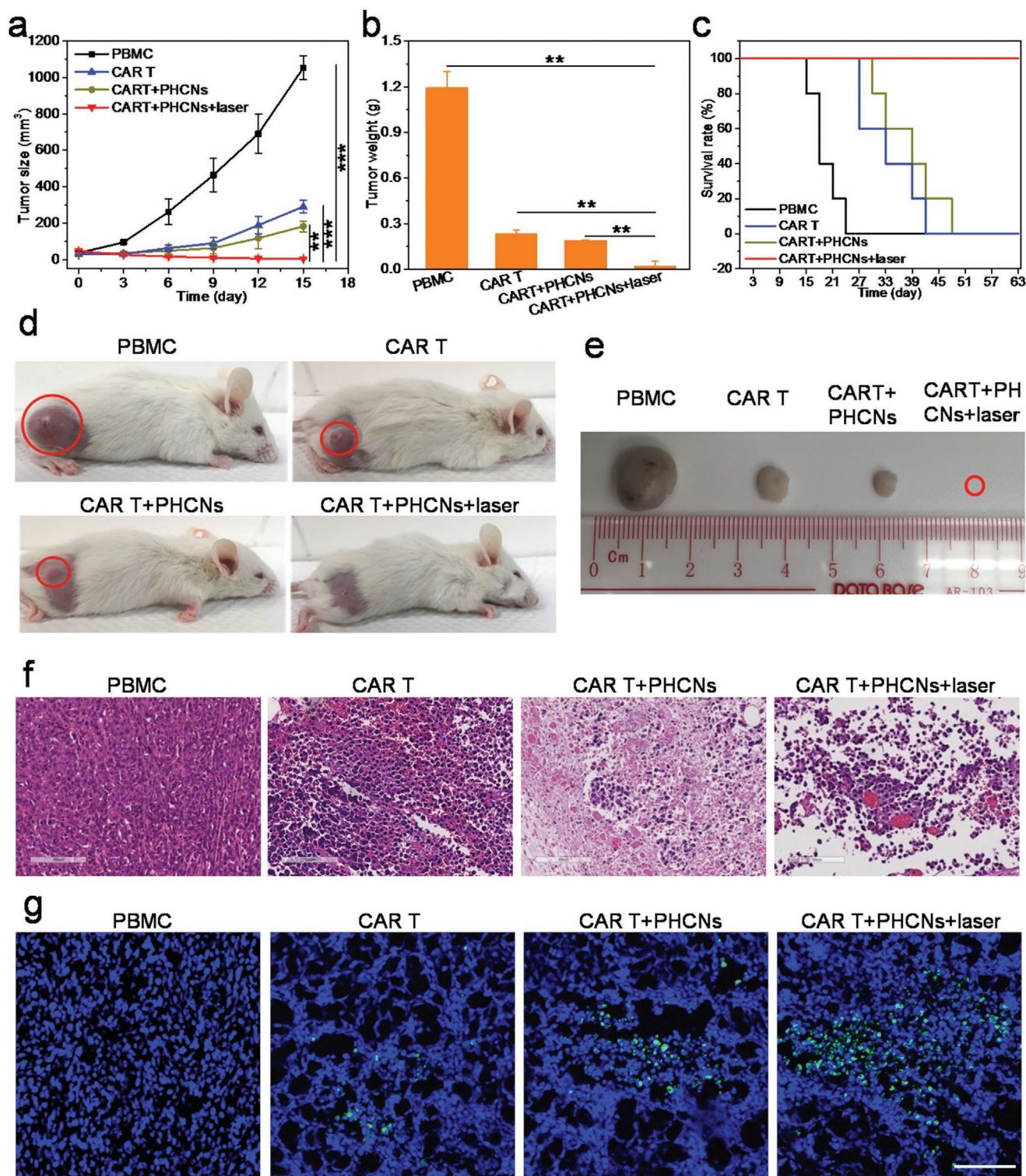


Figure 5. In vivo combination therapy of nanozyme-mediated treatment with B7-H3 CAR T cells. a) Tumor growth curves and b) tumor weights of mice in different groups ($n = 5$, in each group); c) survival rates of mice after different treatments; representative photos of the d) mice and e) tumor from different groups at day 15 after treatment. f) H&E and g) TUNEL staining of tumor slides collected from different groups of mice after treatment. PBMC represents the PBMC-treated group; CAR T represents the CAR T alone treated group; CART+PHCNs represents the CAR T treated group with non-irradiated PHCNs; CART+PHCNs+laser represents the CAR T treated group with PHCNs plus laser treatment. Scale bar: 100 μm . The p values are analyzed using the Log-rank (Mantel-Cox) test. Data are presented as the mean \pm standard error of the mean. * $p < 0.05$, ** $p < 0.01$, *** $p < 0.001$.

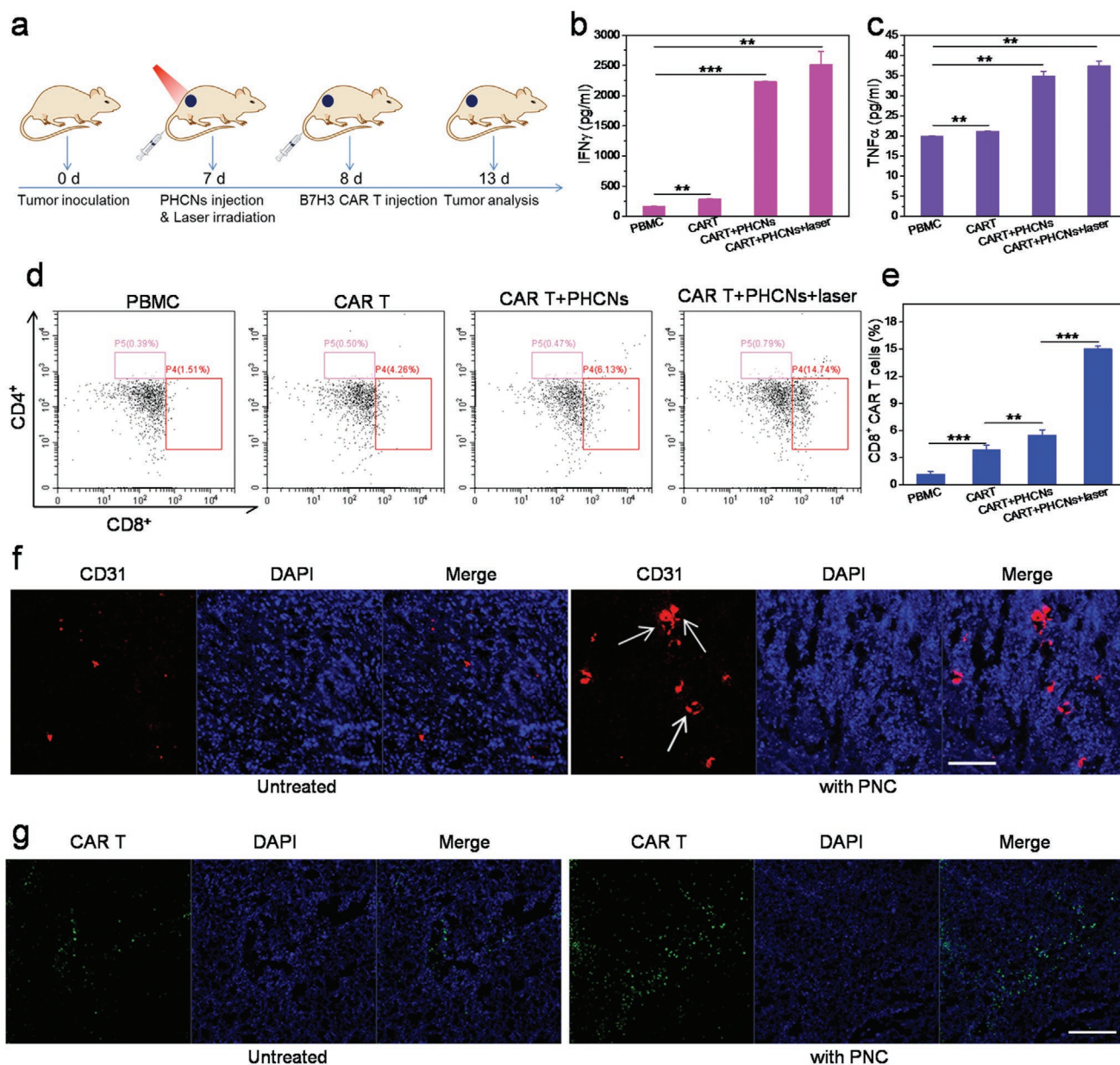


Figure 6. Nanozyme-enhanced in vivo immune activations and infiltrations of B7-H3 CAR T cells by remodeling TME. a) Schematic illustration showing the experimental design of combining nanozyme-mediated PNC therapy and CAR T cell therapy ($n = 5$, in each group). The levels of b) IFN- γ and c) TNF- α detected in mice. Representative flow cytometric plots (d) and statistical analysis (e) of CD8⁺ CAR T cells in tumors measured using the flow cytometry. PBMC represents the PBMC-treated group; CART T represents the CAR T alone treated group; CART+PHCNs represents the CAR T treated group with non-irradiated PHCNs; CART+PHCNs+laser represents the CAR T treated group with PHCNs plus laser treatment. f) Immunofluorescence staining of blood vessels in tumor tissues collected from mice with/without PHCNs plus laser treatment. Scale bar: 100 μ m. g) Immunofluorescence staining of B7-H3 CAR T cells carrying the report gene infiltrating the tumors with/without PHCNs plus laser treatment. Scale bar: 100 μ m. The p values are analyzed using the Log-rank (Mantel-Cox) test. Data are presented as the mean \pm standard error of the mean. * $p < 0.05$, ** $p < 0.01$, *** $p < 0.001$.

3. Conclusion

In summary, our work describes a new nanotechnology approach that can promote CAR T cell therapy for solid tumors. In the study, a tumor-specific nanozyme, PHCN, that transiently resets the TME may improve the success of such treatments. In xenografts, the combination of PHCN and B7-H3 CAR T cell therapy displayed superior antitumor activity, along

with excellent biocompatibility and biosafety. Our studies explore the in vitro and in vivo mechanisms of combination therapy of nanozymes and CAR T cells. Nanozyme-mediated photothermal effect disrupted the tumor extracellular matrix and increased blood perfusion, which increased the infiltration of B7-H3 CAR T cells. High ROS generation by nanozymes enables tumor cells to be more susceptible to CAR T cells and weakens tumor immune resistance. Meanwhile, the release of

tumor-specific antigens by nanozyme-induced PNC effect facilitates the recruitment and activation of antigen-specific CAR T cells in a tumor site. Thus, the combination of nanozyme and CAR T therapy effectively improved the therapeutic index in solid tumors. This strategy provides a promising platform to improve the therapeutic efficacy of CAR T cells against solid tumors simply and safely and highlights great promise in the biomedical field.

4. Experimental Section

Materials: HA (MW 34 kDa) was purchased from Shangdong Freda Biopharm Co., Ltd. Copper (II) chloride (CuCl_2), sodium hydroxide (NaOH), sodium sulfide nonahydrate ($\text{Na}_2\text{S}\cdot 9\text{H}_2\text{O}$), methoxy PEG thiol (mPEG-SH), and hydrazine were obtained from Sigma-Aldrich (USA). Alexa Fluor 488 Annexin V/PI Cell Apoptosis Kit and Calcein-AM/Propidium Iodide (PI) Staining Kit were purchased from Invitrogen (USA). The Cell Counting Kit (CCK-8) was purchased from Shanghai Yeasen Biotechnology Co., Ltd. The Calcein-AM/Propidium Iodide (PI) Staining Kit was purchased from Invitrogen (USA). All other chemicals used were analytical reagent grade and were used without further purification.

Synthesis of PHCNs: In a typical synthesis, CuCl_2 was dissolved in water containing HA, followed by the addition of 25 mL of NaOH. After stirring for 5 min, hydrazine (15 μl) was added to the above mixture. $\text{Na}_2\text{S}\cdot 9\text{H}_2\text{O}$ aqueous stock solution was added to the suspension and heated at 60 °C for 2 h. After the reaction, the HCNs were collected by centrifugation and washed with deionized water for three cycles. Meanwhile, PEGylation was used for surface modification. The obtained PHCNs were mixed with mPEG-SH at room temperature for 48 h and then centrifuged and washed twice with distilled water.

Characterization: The particle size and zeta potential of the nanoparticles could be measured using a Nano-ZS ZEN3600 (Malvern). (UV-vis)-NIR spectral data were determined by using a PerkinElmer Lambda UV spectrophotometer. The crystal structures and phase purities of the samples were investigated by powder XRD with a D8 Focus diffractometer (Bruker) with $\text{Cu K}\alpha$ radiation ($\lambda = 1.5418 \text{ \AA}$) with an operation voltage and current maintained at 40 kV and 40 mA, respectively. The morphologies of the products were determined using a field emission scanning electron microscope (FE-SEM, S-4800, Hitachi). Low-/high-resolution transmission electron microscopy (TEM) was carried out and the composition of samples was determined on an FEI Tecnai G2S-Twin instrument equipped with an energy-dispersive X-ray spectrometer. FT-IR was recorded on a PerkinElmer 580B IR spectrophotometer using the KBr pellet technique. ICP-MS was carried out on a Thermo Fisher X series¹¹.

Photothermal Performance: An aqueous suspension containing PHCNs at different concentrations and laser power densities was exposed to an 808 nm laser with 0.95 W cm^{-2} for 6 min. The temperature variation was monitored using a thermal imaging camera (Fluke). To evaluate the photostability, PHCNs were irradiated for 6 min (laser ON), followed by cooling to room temperature without irradiation for 6 min (laser OFF). Subsequently, additional three ON/OFF cycles were repeated. To investigate the photothermal conversion efficiency, the light from 808 nm laser was applied to the solutions of PHCNs. When the temperature reached plateau, irradiation was discontinued for cooling down to room temperature. A thermal imaging camera was used to monitor the temperature of the solutions during this experiment.

Nanocatalytic Property: To detect generation of extracellular $\cdot\text{OH}$, the PBS solution containing MB was mixed with PHCNs under different H_2O_2 concentrations. The density of $\cdot\text{OH}$ was determined by the absorption at 650 nm. The MB solutions treated with PHCNs or H_2O_2 were used as control groups. In addition, the $\cdot\text{OH}$ generation was measured under different temperature and further tested with/without the laser irradiation.

Besides, the Michaelis-Menten kinetic assay of the PHCNs was examined by changing the concentration of and H_2O_2 . Subsequently, Then TMB oxidation with absorbance at 652 nm ($\text{OD}_{652 \text{ nm}}$) was monitored in real time. Reaction rates (ν) under different concentrations of H_2O_2 were calculated from the initial slope of TMB oxidation. Finally, K_M and V_{max} were calculated through fitting data to Michaelis-Menten saturation curve according to the previously reported method.^[39,40]

Stability: To assess the stability of PHCNs in vitro, the size and zeta potential were measured in various aqueous solutions, including water, and PBS, DMEM medium, and DMEM medium containing 10% FBS.

Cellular Uptake: A549 tumor cells were seeded in the 24-well culture plates (5×10^4 cells per well). After 24-h incubation, PHCNs were added into the wells at different timepoints. Cells were washed with PBS, followed incubation with trypsin. Cells were harvested and lysed using ultrasonication. The copper ions were extracted with nitric acid and sequentially measured using ICP-MS. To observe the effects of HA on cellular uptake, cells were treated with free HA at 37 °C for 2 h, prior to incubation with the nanoparticles, and the copper ions were measured using ICP-MS as described above.

Intracellular ROS Detection: The ROS production in vitro was probed by dichloro-dihydro-fluorescein diacetate (DCFH-DA). Non-fluorescent DCFH-DA can be oxidized by ROS into 2'-7'' dichlorofluorescein (DCF). A549 cells seeded in 24-well plates were treated with PHCNs, following by laser irradiation. DCFH-DA was added and incubated for 15 min. Cells were washed with PBS three times. The fluorescence intensity was detected by Beckman CytoFlex flow cytometry.

In Vitro Cellular Experiments of PHCNs: To measure nanocatalytic efficiency of PHCNs, A549 tumor cells and human umbilical vein endothelial cells (HUVECs) were seeded in the 96-well plates at a density of 1×10^4 cells per well and incubated overnight. PHCNs at different concentrations were added and incubated for 24 h. CCK-8 (10 μL per well) was added to the plates. After incubation for 1.5 h, the absorbance was measured at 450 nm by a microplate reader (Molecular Devices).

To measure antitumor efficiency of PHCNs, A549 tumor cells were pre-incubated with PHCNs in the 96-well plate. Cells were irradiated with an 808 nm laser. Cell viability was measured using the CCK-8 assay as described above. To detect apoptosis, tumor cells were stained with Calcein-AM/PI kit according to the manufacturer's instruction. The cells were stained with Calcein-AM for live cells and PI for dead/late apoptotic cells. Finally, the cells were observed with inverted microscope (Olympus IX71, JPN).

In Vitro Combination Therapy of PHCNs and CAR T Cells: Cytotoxicity of CAR T cells was measured using the Calcein-AM release method. A549 tumor cells at 1×10^5 cells mL^{-1} were incubated with Calcein-AM for 30 min at 37 °C. After washing, A549 cells were seeded in the 24-well plates. Then PHCNs were added, following by laser irradiation. After washing, B7-H3 CAR T cells were added at different E:T ratios and incubated for 24 h. To assess the cell lysis rate, Calcein-AM in the supernatant released from lysated cells was measured using a microplate reader. To analyze the activation of CAR T cells, the production levels of key cytokines (IFN- γ , TNF- α , granzyme-B, and perforin) released from CAR T cells in the culture supernatants was measured using BD Cytometric Bead Array (CBA) Human Th1/Th2 Cytokine Kit II (BD Biosciences) following the manufacture's instruction. To analyze subtypes of CAR T cells, cells were stained with anti-CD3-APC (Biolegend) and anti-CD8a-PE-Cy7 (Biolegend) antibodies. All samples were analyzed using the CytoFlex S (Beckman Coulter) flow cytometry.

For T cell proliferation assay, CAR T cells were prestained with CellTrace Far Red Cell Proliferation Kit according to the manufacturer's protocol. A549 cells were treated with/without PHCNs and co-cultured with CAR T cells. After 24 h, the CAR T cells were collected, centrifugated, and resuspended in PBS. The cell proliferation was analyzed by flow cytometry.

In Vivo Combination Therapy: The study was conducted according to the guideline of Institutional Animal Care and Use Committee. All animal experimental protocols were approved by the Institutional Animal Care and Use Committee, University of Macau. The approval number was UMARE-041-2020. Tumor xenografts were established by

subcutaneous inoculation of 2×10^6 A549 tumor cells. All mice were used for experiments when the tumors reached the size of around 50 mm^3 . NOD/SCID mice were randomly divided into four groups ($n = 5$, in each group) including: 1) PBMC, 2) CAR T cells, 3) CAR T cells plus PHCNs, and 4) CAR T cells plus PHCNs under laser irradiation (PNC). After intravenous administration of PHCNs for 12 h, the tumor sites were irradiated with the 808 nm laser (0.95 W cm^{-2} , 6 min). After 12 h, 0.5×10^7 B7-H3 CAR T cells were then intravenously administered. The body weights and tumor sizes were measured every 3 days using an electronic balance and a caliper, respectively. Tumor volumes were calculated using equations $V = [(length) \times (width)^2]/2$. After treatments, the tumors were collected, sectioned, and stained with H&E and TUNEL.

In Vivo Dual-Modal Tumor Imaging: For in vivo PA imaging, PHCNs were injected into A549-xenografted mice via intravenous administration. Then, PA imaging was performed at 0, 6, 12, and 24 h post-injection using the PA equipment (Endra Nexus 128, MI).

For in vivo photothermal imaging, A549-xenografted mice were intravenously injected with PHCNs. After 12 h, the tumor sites were exposed to an 808 nm laser (0.95 W cm^{-2} , 6 min). During the NIR irradiation, the infrared thermal camera was used to monitor the temperature changes of the tumor areas.

Immune Response Analysis in TME: To analyze the CAR T cells in the TME, the tumor tissues were harvested from mice in different treatment groups, and digested using collagenase, hyaluronidase, and DNase at 37°C for 1 h. Immune cells were filtered through nylon mesh filters and washed with PBS containing 3% FBS. The CAR T cells were detected with anti-CD3-APC (Biolegend), anti-CD4-PE (Biolegend), and anti-CD8a-PE-Cy7 (Biolegend) antibodies. All samples were analyzed using the CytoFlex S (Beckman Coulter) flow cytometry.

Immunofluorescence Staining in Tumor Tissues: Tumor-bearing mice were intravenously injected with the PHCNs. After 12 h injection, the tumor sites were irradiated with the 808 nm laser (0.95 W cm^{-2} , 6 min). Then, these tumors were surgically excised for immunofluorescence staining. Next, frozen sections of the tumors were prepared with optimum cutting temperature (OCT) compound. Staining of blood vessels was done by incubation with mouse Alexa Fluor 647-anti-CD31 monoclonal antibody (dilution 1:200, Biolegend). Cell nuclei were stained with DAPI. The stained tumor sections were imaged under confocal fluorescence microscopy (Leica SP5).

The tumor-bearing mice were intravenously injected with the PHCNs. After 12 h injection, the mice were anesthetized and the tumors were irradiated with the 808 nm laser (0.95 W cm^{-2} , 6 min). After treatment, 0.5×10^7 B7-H3 CAR T cells carrying the report gene were intravenously administered. Then, these tumors were surgically excised for immunofluorescence staining. Next, frozen sections of the tumors were prepared with OCT compound. Tumor tissues were sectioned into $10 \mu\text{m}$ slices, and cell nuclei were stained with DAPI. The stained tumor sections were imaged under confocal fluorescence microscopy (Leica SP5).

For in vivo tumor blood flow rate detecting, PHCNs were injected into A549-xenografted mice via intravenous administration. After 12 h injection, the mice were anesthetized and the tumors were irradiated. Then, flow rate detecting was performed around tumor region at pretreatment and 0, 12, 24 h after irradiation using the laser speckle equipment.

In Vivo Biodistribution: Tumor Xenografts were injected with PHCNs. The major organs, including heart, liver, spleen, lung, kidney, and tumor, were collected at different time points. The organs were treated with nitric acid and H_2O_2 ($v/v = 1:2$) until the solutions became clear. The concentrations of copper collected from the organs were measured by ICP-MS.

In Vivo Biocompatible Evaluation: Serum levels of AST and ALT were measured after post-injection by the commercial kits. Meanwhile, the major organs (heart, liver, spleen, lung, and kidney) were harvested and fixed using paraformaldehyde. Tissue samples were then embedded in paraffin, sliced, and stained using H&E. The histological sections were observed under an optical microscope.

Statistical Analysis: All statistical analyses were performed using GraphPad Prism software. Significant differences were calculated using

the Log-rank (Mantel-Cox) test. *P* values are represented as: * $p < 0.05$, ** $p < 0.01$, and *** $p < 0.001$.

Supporting Information

Supporting Information is available from the Wiley Online Library or from the author.

Acknowledgements

L.Z. and J.L. contributed equally to this work. This work is supported by the National Key R&D Program of China (2019YFA0904400), the Science and Technology Development Fund of Macau (File no. FDCT/131/2016/A3, FDCT/0015/2018/A1), National Natural Science Foundation of China (31440041), and the Intramural Research Program of Faculty of Health Sciences, University of Macau (File no. MYRG2019-00069-FHS, SRG2016-00082-FHS). We thanks for the assistance of Prof. Wenhua Zheng (University of Macau).

Conflict of Interest

The authors declare no conflict of interest.

Data Availability Statement

Research data are not shared.

Keywords

B7-H3 immune checkpoint, chimeric antigen receptor T cell, immunotherapy, nanozyme, photothermal-nanocatalytic effect

Received: May 4, 2021

Revised: June 7, 2021

Published online:

- [1] R. G. Majzner, J. L. Theruvath, A. Nellan, S. Heitzeneder, Y. Cui, C. W. Mount, S. P. Rietberg, M. H. Linde, P. Xu, C. Rota, E. Sotillo, L. Labanieh, D. W. Lee, R. J. Orentas, D. S. Dimitrov, Z. Zhu, B. St. Croix, A. Delaidelli, A. Sekunova, E. Bonvini, S. S. Mitra, M. M. Quezado, R. Majeti, M. Monje, P. H. B. Sorensen, J. M. Maris, C. L. Mackall, *Clin. Cancer Res.* **2019**, *25*, 2560.
- [2] H. Du, K. Hirabayashi, S. Ahn, N. P. Kren, S. A. Montgomery, X. Wang, K. Tiruthani, B. Mirlekar, D. Michaud, K. Greene, S. G. Herrera, Y. Xu, C. Sun, Y. Chen, X. Ma, C. R. Ferrone, Y. Pylayeva-Gupta, J. J. Yeh, R. Liu, B. Savoldo, S. Ferrone, G. Dotti, *Cancer Cell* **2019**, *35*, 221.
- [3] X. Tang, S. Zhao, Y. Zhang, Y. Wang, Z. Zhang, M. Yang, Y. Zhu, G. Zhang, G. Guo, A. Tong, L. Zhou, *Mol. Ther.–Oncolytics* **2019**, *14*, 279.
- [4] S. Yang, B. Cao, G. Zhou, L. Zhu, L. Wang, L. Zhang, H. F. Kwok, Z. Zhang, Q. Zhao, *Front. Pharmacol.* **2020**, *11*, 1089.
- [5] L. Zhu, J. Liu, G. Zhou, H. M. Ng, I. L. Ang, G. Ma, Y. Liu, S. Yang, F. Zhang, K. Miao, T. C. W. Poon, X. Zhang, Z. Yuan, C.-X. Deng, Q. Zhao, *Chem. Commun.* **2019**, *55*, 14255.
- [6] H. Kaplon, M. Muralidharan, Z. Schneider, J. M. Reichert, *mAbs* **2020**, *12*, 1703531.

- [7] A. D. Fesnak, C. H. June, B. L. Levine, *Nat. Rev. Cancer* **2016**, *16*, 566.
- [8] M. Ahmed, M. Cheng, Q. Zhao, Y. Goldgur, S. M. Cheal, H.-F. Guo, S. M. Larson, N.-K. V. Cheung, *J. Biol. Chem.* **2015**, *290*, 30018.
- [9] J. Liu, G. Zhou, L. Zhang, Q. Zhao, *Front. Immunol.* **2019**, *10*, 456.
- [10] J. Liu, S. Yang, B. Cao, G. Zhou, F. Zhang, Y. Wang, R. Wang, L. Zhu, Y. Meng, C. Hu, H. Liang, X. Lin, K. Zhu, G. Chen, K. Q. Luo, L. Di, Q. Zhao, *J. Hematol. Oncol.* **2021**, *14*, 21.
- [11] S. A. Richman, S. Nunez-Cruz, B. Moghimi, L. Z. Li, Z. T. Gershenson, Z. Mourelatos, D. M. Barrett, S. A. Grupp, M. C. Milone, *Cancer Immunol. Res.* **2018**, *6*, 36.
- [12] C. H. Lamers, S. Sleijfer, S. Van Steenbergen, P. Van Elzakker, B. Van Krimpen, C. Groot, A. Vulto, M. Den Bakker, E. Oosterwijk, R. Debets, J. W. Gratama, *Mol. Ther.* **2013**, *21*, 904.
- [13] E. Donnadieu, L. Dupré, L. G. Pinho, V. Cotta-De-Almeida, *J. Leukocyte Biol.* **2020**, *108*, 1067.
- [14] C. Feig, J. O. Jones, M. Kraman, R. J. B. Wells, A. Deonarine, D. S. Chan, C. M. Connell, E. W. Roberts, Q. Zhao, O. L. Caballero, S. A. Teichmann, T. Janowitz, D. I. Jodrell, D. A. Tuveson, D. T. Fearon, *Proc. Natl. Acad. Sci. U. S. A.* **2013**, *110*, 20212.
- [15] M. V. Maus, A. R. Haas, G. L. Beatty, S. M. Albelda, B. L. Levine, X. Liu, Y. Zhao, M. Kalos, C. H. June, *Cancer Immunol. Res.* **2013**, *1*, 26.
- [16] K. Newick, S. O'Brien, E. Moon, S. M. Albelda, *Annu. Rev. Med.* **2017**, *68*, 139.
- [17] I. Caruana, B. Savoldo, V. Hoyos, G. Weber, H. Liu, E. S. Kim, M. M. Ittmann, D. Marchetti, G. Dotti, *Nat. Med.* **2015**, *21*, 524.
- [18] R. K. Jain, T. Stylianopoulos, *Nat. Rev. Clin. Oncol.* **2010**, *7*, 653.
- [19] S. Tahmasebi, R. Elahi, A. Esmaeilzadeh, *Stem Cell Rev. Rep.* **2019**, *15*, 619.
- [20] J. Henze, F. Tacke, O. Hardt, F. Alves, W. Al Rawashdeh, *Cancers* **2020**, *12*, 1389.
- [21] S. Rafiq, C. S. Hackett, R. J. Brentjens, *Nat. Rev. Clin. Oncol.* **2020**, *17*, 147.
- [22] Q. Chen, Q. Hu, E. Dukhovlina, G. Chen, S. Ahn, C. Wang, E. A. Ogunnaike, F. S. Ligler, G. Dotti, Z. Gu, *Adv. Mater.* **2019**, *31*, 1900192.
- [23] F. Zhang, S. B. Stephan, C. I. Ene, T. T. Smith, E. C. Holland, M. T. Stephan, *Cancer Res.* **2018**, *78*, 3718.
- [24] Z. Chen, H. Pan, Y. Luo, T. Yin, B. Zhang, J. Liao, M. Wang, X. Tang, G. Huang, G. Deng, M. Zheng, L. Cai, *Small* **2021**, *17*, 2007494.
- [25] L. Zhu, D. Gao, L. Xie, Y. Dai, Q. Zhao, *Mol. Pharm.* **2020**, *17*, 3720.
- [26] B. Yang, Y. Chen, J. Shi, *Adv. Mater.* **2019**, *31*, 1901778.
- [27] F. Liu, L. Lin, Y. Zhang, Y. Wang, S. Sheng, C. Xu, H. Tian, X. Chen, *Adv. Mater.* **2019**, *31*, 1902885.
- [28] B. Xu, Y. Cui, W. Wang, S. Li, C. Lyu, S. Wang, W. Bao, H. Wang, M. Qin, Z. Liu, W. Wei, H. Liu, *Adv. Mater.* **2020**, *32*, 2003563.
- [29] Z. Wang, Z. Li, Z. Sun, S. Wang, Z. Ali, S. Zhu, S. Liu, Q. Ren, F. Sheng, B. Wang, Y. Hou, *Sci. Adv.* **2020**, *6*, eabc8733.
- [30] M. B. Gawande, A. Goswami, F.-X. Felpin, T. Asefa, X. Huang, R. Silva, X. Zou, R. Zboril, R. S. Varma, *Chem. Rev.* **2016**, *116*, 3722.
- [31] P. Chen, Y. Ma, Z. Zheng, C. Wu, Y. Wang, G. Liang, *Nat. Commun.* **2019**, *10*, 1192.
- [32] W. Fan, B. Yung, P. Huang, X. Chen, *Chem. Rev.* **2017**, *117*, 13566.
- [33] K. Yang, H. Xu, L. Cheng, C. Sun, J. Wang, Z. Liu, *Adv. Mater.* **2012**, *24*, 5586.
- [34] J. T. Robinson, S. M. Tabakman, Y. Liang, H. Wang, H. Sanchez Casalongue, D. Vinh, H. Dai, *J. Am. Chem. Soc.* **2011**, *133*, 6825.
- [35] Z. Zhao, C. Chen, W. Wu, F. Wang, L. Du, X. Zhang, Y. Xiong, X. He, Y. Cai, R. T. K. Kwok, J. W. Y. Lam, X. Gao, P. Sun, D. L. Phillips, D. Ding, B. Z. Tang, *Nat. Commun.* **2019**, *10*, 768.
- [36] G. Mattheolabakis, L. Milane, A. Singh, M. M. Amiji, *J. Drug Targeting* **2015**, *23*, 605.
- [37] H. He, Y. Bai, J. Wang, Q. Deng, L. Zhu, F. Meng, Z. Zhong, L. Yin, *Biomacromolecules* **2015**, *16*, 1390.
- [38] C. L. Bonifant, H. J. Jackson, R. J. Brentjens, K. J. Curran, *Mol. Ther.—Oncolytics* **2016**, *3*, 16011.
- [39] S. Li, L. Shang, B. Xu, S. Wang, K. Gu, Q. Wu, Y. Sun, Q. Zhang, H. Yang, F. Zhang, L. Gu, T. Zhang, H. Liu, *Angew. Chem., Int. Ed. Engl.* **2019**, *58*, 12624.
- [40] J. Xi, G. Wei, L. An, Z. Xu, Z. Xu, L. Fan, L. Gao, *Nano Lett.* **2019**, *19*, 7645.